Inducing Synergy in Bimetallic RhNi Catalysts for CO_2 Methanation by Galvanic Replacement

Yuan Wang,[a,b,c] Hamidreza Arandiyan,[d,*] Stuart A. Bartlett,[d] Annette Trunschke,[c,*] Hongyu Sun,[e] Jason Scott,[a,*] Adam F. Lee,[f,*] Karen Wilson,[f] Thomas Maschmeyer,[d] Robert Schlögl,[c] and Rose Amal[a]

Dr. Yuan Wang, A/Prof. Jason Scott, and Prof. Rose Amal

[a] *Particles and Catalysis Research Group, School of Chemical Engineering, The University of New South Wales, Sydney 2052, Australia*

Dr. Yuan Wang

[b] *School of Chemistry, Faculty of Science, The University of New South Wales, Sydney, New South Wales, Australia*

Dr. Annette Trunschke, Dr. Yuan Wang and Prof. Robert Schlögl

[c] *Inorganic Chemistry Department, Fritz-Haber-Institut der Max-Planck-Gesellschaft, Faradayweg 4-6, 14195 Berlin, Germany*

Dr. Hamidreza Arandiyan, Dr. Stuart A. Bartlett, and Prof. Thomas Maschmeyer

[d] *Laboratory of Advanced Catalysis for Sustainability, School of Chemistry, The University of Sydney, Sydney 2006, Australia*

Dr. Hongyu Sun

[e] *Department of Micro- and Nanotechnology, Technical University of Denmark, Kongens Lyngby 2800, Denmark*

Prof. Karen Wilson, and Prof. Adam F. Lee

[f] *School of Science, Royal Melbourne Institute of Technology University, Melbourne, VIC 3000, Australia*

** Corresponding authors E-mail address: hamid.arandiyan@sydney.edu.au (H.A.), adam.lee2@rmit.edu.au (A.F.L.) jason.scott@unsw.edu.au (J.S.), trunschke@fhi-berlin.mpg.de (A.T.)*

Abstract

CO_2 utilisation as a chemical feedstock could transform fuels production and help mitigate climate change. Direct CO_2 reduction for energy production requires the development of active, stable, and low-cost catalysts selective for methane. A bimetallic Ni@Rh core-shell catalyst prepared by galvanic replacement (GR) exhibits a 3.5-fold rate enhancement for CO_2 methanation relative to an analogue prepared by chemical reduction (CR) and is twice as active as monometallic Rh/Al_2O_3. Superior performance of $RhNi/Al_2O_3$ (GR) is attributed to Rh dispersion as an atomically thin RhO_x shell encapsulating Ni nanoparticles, stabilised by a strong Rh-Ni interaction. Operando IR spectroscopy identifies reactively-formed CO from the dissociative chemisorption of CO_2 over Rh as the key intermediate for methane production. Surface formate from the dissociative chemisorption of CO_2 and subsequent hydrogenation (via spillover from Rh sites) over alumina is a catalytic spectator. This mechanistic insight paves the way to high activity nanostructured catalysts for CO_2 methanation.

Keywords: Bimetallic; nanoparticle; galvanic replacement; CO_2; methane

1. Introduction

The addition of one metal to another, to form a bimetallic material, often modifies the resulting structural, electronic, and catalytic properties of the parent element.[1] In regard of catalysis by bimetallic nanoparticles (NPs), such changes may arise from new particle morphologies, surface terminations and active site ensembles (so-called geometric or structural effects), and/or charge transfer between the constituent metals and associated modified electronic band structure and metal-support interactions (so-called electronic or ligand effects).[2] For instance, the catalytic hydrogenation of levulinic acid compared over $Au-Pd/TiO_2$ prepared by wet impregnation is accelerated 27-fold compared with monometallic counterparts,[3] while Au surfaces alloying with Pd increased activity and selectivity for ethyne cyclotrimerization to benzene over Au@Pd colloids;[4] in both cases, superior performance is ascribed to the break-up of Pd ensembles by Au. Zin et al [5] used a novel emulsion-assisted, ethylene glycol ternary system to synthesise monodispersed bimetallic Pd-Ag NPs on carbon black which demonstrated an activity comparable to commercial Pt/C catalyst for methanol oxidation in an alkaline medium. Bimetallic Au-Pd alloy NPs dispersed on nanohybrid three-dimensionally ordered macroporous $La_{0.6}Sr_{0.4}MnO_3$ (3DOM LSMO) perovskite catalysts also exhibited enhanced activity for low temperature methane combustion relative to monometallic Au and Pd catalysts.[6] In-situ diffuse reflectance infrared Fourier transform spectroscopy (DRIFTS) of the AuPd/3DOM LSMO revealed that Au changed the reaction pathway by increasing the concentration of adsorbed oxygen species and weakening binding between reactive intermediates and Pd.[6] Such synergies are strongly dependent on the precise nature of metal-metal

interactions, however control over the morphology, composition, and elemental distribution of bimetallic nanoparticles remains challenging, hindering the rational prediction of catalytic reactivity.[7] In lignin hydrogenolysis, Yan et al[8] reported that Ru-Ni displayed the highest activity for C-O bond cleavage among bimetallic Ni-M catalysts (M = Ru, Rh, Pd) and was also significantly more active than pure Ni and Ru catalysts for the direct conversion of lignin to monomeric aromatic chemicals. A bimetallic Au@Rh core-shell nanodendrite fabricated by a one-pot hydrothermal method[9] provides an example where morphology dominates reactivity; the bimetallic catalyst outperforming a monometallic Rh nanodendrite and commercial Rh nanocatalyst for hydrogen generation from hydrazine.

With the emergence of abundant, low cost H_2 from electrolysis using renewable energy, catalytic hydrogenation of CO_2 into chemical products and fuels now offers an economically viable non-fossil route to hydrocarbons (the power-to-gas-concept),[10] and opportunity to mitigate anthropogenic CO_2 emissions. There are 95 commercial power-to-gas projects currently operational worldwide, with a combined output of 39 MW electricity;[10] even modest improvements in catalyst performance could therefore have a significant impact on reducing environmental greenhouse gas emissions while strengthening the global energy landscape. CO_2 reduction by H_2 to methane (methanation) may employ either precious (e.g. Rh, Ru, Pd and Pt) or transition (e.g. Ni, Co, Ce, Cr and Zr) metals[11-13], with activity decreasing in the order Ru > Rh > Ni > Co > Pt > Pd and selectivity Pd > Pt > Ir > Ni > Rh > Co > Fe > Ru > Mo > Ag > Au.[14] Supported bimetallic Rh–Ni catalysts are also reported active for CO_2 methanation,[15] although the origin of their superior turnover frequency relative to monometallic Rh, and the role of support, remains poorly understood. CO_2 methanation can proceed through either CO or formate routes, depending on the choice of metal(s), their morphology, and support. For example, Christopher et al[16] found that isolated atoms and nanoparticles of Rh exhibited different catalytic selectivity for CO_2 reduction, while Bentrup and co-workers[17] noted that Ni and K additives can tune the strength of CO adsorption and rate of H_2 activation over Rh/Al_2O_3. Swalus et al[18] also observed a synergy between a physical mixture of Ni/C and Rh/Al_2O_3, attributed to a bifunctional mechanism involving hydrogen dissociation and spillover from Ni to Rh, although evidence of this remains scarce. Subnanometer Rh clusters derived from Rh-doped $SrTiO_3$ by a doping-segregation method are highly active for CO_2 reduction wherein strong interactions between Rh atoms and the defective oxide support promote CO_2 activation and enhance CO selectivity.[19] Despite substantial efforts,[20, 21] the role of catalytic sites and the precise reaction mechanism(s) for CO_2 methanation over bimetallic Rh-Ni catalysts remain elusive. In particular, whether CO_2 methanation requires a CO intermediate[22] or can proceed directly to methane without in-situ CO formation,[23] and in the former case, whether CO is formed by CO_2 dissociation[24] or from a formate intermediate by the reverse water gas shift reaction.[25]

We recently demonstrated that in-situ exsolution of Ni from a Rh/3DOM $LaNi_{0.08}Al_{0.92}O_3$ perovskite resulted in the formation of bimetallic alloy nanoparticles. Herein, we explore the use of galvanic replacement to induce intimate

contact between Rh and Ni without their alloying, and the application of advanced in-situ and operando IR spectroscopies to elucidate the roles of metal and support and thereby identify the major reaction pathway in CO_2 hydrogenation to methane. Alumina was selected as an inert support in galvanic replacement, unlike e.g. Mn_3O_4,[26] and one that is not expected to exhibit strong metal-support interactions and influence the structure of deposited Rh-Ni NPs. Galvanic replacement enables the design of a Ni@Rh core-shell catalyst wherein Rh atoms are highly dispersed, offering high selectivity for CO_2 methanation with an activity four times that achievable over RhNi bimetallic alloys.

2. Experimental

2.1. Ni/Al_2O_3, Rh/Al_2O_3 and $RhNi/Al_2O_3$ (CR) preparation by chemical reduction

The preparation of Ni and Rh, and bimetallic Rh-Ni supported on Al_2O_3 (Sigma Aldrich) (namely Ni/Al_2O_3, Rh/Al_2O_3 and $RhNi/Al_2O_3$ (CR)) followed previously reported procedures.[6] Al_2O_3 powder was added to a $Ni(NO_3)_2{\cdot}6H_2O$ and/or $RhCl_3{\cdot}xH_2O$ aqueous solution containing polyvinyl alcohol (PVA, M_W 89,000-98,000; Ni:PVA mass ratio=1:1.5) and magnetically stirred for 20 min. A reducing agent (0.1 M $NaBH_4$) was then rapidly added to the suspension solution to give a 5:1 molar ratio of Na:Ni. The suspension was stirred for a further 30 min before being filtered and washed with 500 mL distilled water and 500 mL ethanol. It was then dried at 80 °C for 12 h. The recovered solid was calcined at 450 °C in Muffle furnace (ramp rate = 5 °C/min) for 3 h and then cooled to room temperature to remove the PVA capping agent. Each sample was activated by reducing at 400 °C (ramp rate = 5 °C/min) in a 25 mL/min H_2 flow for 1 h.

2.2. $RhNi/Al_2O_3$ (GR) preparation by galvanic replacement reaction

The method described by Lu et al was used as the basis for the galvanic replacement (GR) process to prepare the bimetallic $RhNi/Al_2O_3$ (GR) catalyst.[27] As the Ni precursor has a lower reduction potential (Ni^{2+}/Ni, E^0 = -0.25 V) than Rh (Rh^{3+}/Rh, E^0 = +0.76 V) it is favourable for Rh (III) precursors to be reduced by the Ni host metal via the following displacement reaction:

$$3Ni + 2Rh^{3+} \rightarrow 3Ni^{2+} + 2Rh \ (\Delta E^0 = +0.46 \text{ V})$$

A typical procedure was as follows (**Scheme 1**): the obtained Ni/Al_2O_3 was prereduced again in the same condition (400 °C, 5 °C/min in a 25 mL/min H_2 flow for 1 h) before used as Ni precursor to ensure the Ni is in metallic state. Then Ni/Al_2O_3 was mixed with a desired amount of $RhCl_3{\cdot}xH_2O$ in an aqueous solution and under an N_2 environment in a three-neck round bottom flask. After stirring for 2 h, the solid was collected via filtration and washed with distilled water and ethanol several times before drying at 80 °C for 12 h. The solid was then reduced in H_2 (flow rate = 25 mL/min) at 400 °C (ramp rate = 5 °C/min) for 1 h. $RhNi/Al_2O_3$ (GR) prepared with different Rh precursor solution concentrations of $2.98\times10^{-}$

^{4}, 5.84×10^{-4}, 8.60×10^{-4} and 11.3×10^{-4} M are denoted as Rh-Ni GR-1, Rh-Ni GR-2, Rh-Ni GR-3, and Rh-Ni GR-4 (within Supporting Information), respectively. Rh-Ni GR-3 gave the best catalytic performance for the CO_2 reduction reaction and was therefore selected for the detailed characterisation studies. Within the main text, $RhNi/Al_2O_3$ (GR) refers to Rh-Ni GR-3.

2.3. Characterisation

Bulk and surface physicochemical properties of materials were studied by XRD, HRTEM, HAADF-STEM, EDS, N_2 physisorption, H_2-TPR, XPS, XAS and ICP-MS; instrument details and experimental protocols are provided in the Supporting Information.

2.4. In-situ Fourier transform infrared (FTIR) spectroscopy of adsorbed CO

FTIR spectra in transmission mode were recorded using a Perkin-Elmer Spectrum 100 FTIR spectrometer equipped with a nitrogen-cooled MCT detector as shown in **Fig. S1**. Spectra were recorded at a resolution of 2 cm^{-1} with accumulation of 64 scans and normalised by dividing the recorded intensities by the corresponding pellet weight area (mg/mm^2). Approximately 20 mg of the powder sample was pressed into a wafer (**Fig. S2**) and placed into a quartz IR cell, which allows adsorption at beam temperature and liquid-nitrogen temperature after thermal treatment under a controlled atmosphere. Prior to CO adsorption the catalysts were reduced in-situ. During the reduction process, the samples were treated in H_2 (0.05 MPa) at 400 °C (heating rate 10 °C/min) for 2 h with 3-4 intermediate evacuations to remove reactively-formed water. Once reduced, the samples were cooled to room temperature under vacuum. In the final step, the pre-treated samples were subjected to the probe adsorption. For the experiments involving adsorption at 77 K, He was admitted to the cell up to an equilibrium pressure of 0.0002 MPa at room temperature before cooling to 77 K. A spectrum of the empty cell (at 77 K) served as a background for the measurements. The probe molecule (CO) was adsorbed from low CO amount and gradually increased to CO saturation (p_{CO} = 0-0.001 MPa). After the adsorption process (at 77 K), the cell was flushed three times with 0.004 MPa He to remove residual gas phase CO. The spectra were recorded when the temperature increased from 77 K to room temperature at an equilibrium pressure of 0.0002 MPa He.

2.5. In-situ diffuse reflectance infrared Fourier transform spectroscopy (DRIFTS)

In-situ DRIFTS was undertaken using an Agilent Technologies Cary 600 Series FTIR Spectrometer, equipped with a liquid N_2 cooled MCT detector at a spectral resolution of 2 cm^{-1} and accumulation of 256 scans. KBr optics windows were applied. For each analysis, approximately 30 mg of catalyst was placed in an in-situ Harrick Praying Mantis^{TM} diffuse reflectance attachment DRP-DF8 cell in combination with a low temperature CHC-CHA-3 reaction chamber. Prior to measurement, the sample was treated in H_2 at 400 °C for 1 h to remove residual of impurities and moisture on the catalyst

surface and reduce the metal oxide nanoparticles. The sample was then cooled to room temperature (RT) for DRIFTS analysis. Spectra were taken from 30 to 400 °C at 2 °C/min every 5 min in both Ar flow (40 mL/min) and the reaction gas flow (CO_2:H_2:Ar=2:8:30, 40 mL/min total). Spectra are presented in Kubelka–Munk units $F(R_\infty) = (1 - R_\infty)^2/2R_\infty$ from the division of spectra taken under reaction gas to the spectra taken under an Ar flow in each corresponding temperature. The outlet gas from IR cell was analysed using a micro-GC (VARIAN, cp-4900) to monitor reaction.

2.6. CO_2 methanation

Catalytic activity for CO_2 methanation was evaluated in a continuous-flow fixed-bed quartz tube microreactor (i.d. = 6.0 mm) at atmospheric pressure (**Fig. S3**). Approximately 50 mg of catalyst was packed in a reactor and initially reduced at 400 °C in a 25 mL/min H_2 flow for 1 h. Next, the sample was with a flow of N_2 (25 mL/min) for 30 min while cooling from 450 to 150 °C. Following catalyst pre-treatment, the reactant gas containing 5 % CO_2: 20 % H_2: 75 % N_2 was passed through the reactor bed at a total flow rate of 40 mL/min, giving a GHSV of ca. 48,000 mL/(g h). The outlet gases were analysed online by a gas chromatograph (Young Lin 6500) equipped with a TCD and a Carboxen-1010 PLOT column. CH_4 and CO were the only carbon containing products detected over any catalysts (see Supplementary Information), and hence CO_2 conversion, CH_4 and CO selectivities, and carbon mass balance were calculated using the following formulas:

$$\text{Conversion of } CO_2\ (\%) = \frac{[CO_2]_{in} - [CO_2]_{out}}{[CO_2]_{in}} \times 100\%$$

$$\text{Selectivity to } CH_4\ (\%) = \frac{[CH_4]_{out}}{[CH_4]_{out} + [CO]_{out}} \times 100\%$$

$$\text{Selectivity to } CO\ (\%) = \frac{[CO]_{out}}{[CH_4]_{out} + [CO]_{out}} \times 100\%$$

$$\text{Carbon mass balance}\ (\%) = \frac{[CH_4]_{out} + [CO]_{out}}{[CO_2]_{in} - [CO_2]_{out}} \times 100\%$$

where $[CO_2]_{in}$ and $[CO_2]_{out}$ are the concentrations of CO_2 at the inlet and outlet, respectively; $[CH_4]_{out}$ and $[CO]_{out}$ are the concentrations of CH_4 and CO, respectively, at the outlet.

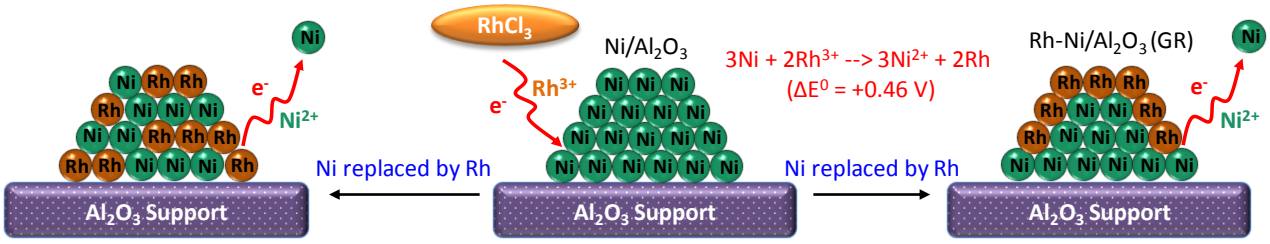

Scheme 1. Possible structures of as-prepared bimetallic $RhNi/Al_2O_3$ catalysts synthesised by galvanic replacement.

3. Results and Discussion

3.1. Characterisation of Rh-Ni catalysts

High-angle annular dark-field scanning transmission electron microscopy (HAADF-STEM) of Rh/Al_2O_3 (**Fig. 1a, b**) and $RhNi/Al_2O_3$ (GR) (**Fig. 1c, d**) evidenced highly dispersed, and relatively uniform, metal NPs in both cases with mean diameters of 1.0 nm and 1.2 nm respectively (**Fig. S4** and **Fig. S5**). In contrast, $RhNi/Al_2O_3$ (CR) possessed a larger mean metal NP sizes of 1.3 nm, with some large Ni NP agglomerates apparent (**Fig. S6**). The lattice fringes of the Rh NP in Rh/Al_2O_3 exhibit *d* spacings of 0.22 nm (**Fig. 1b**), which can be indexed to the (111) plane of fcc Rh, while those of Rh-Ni NPs possessed a slightly smaller *d* spacing value of 0.21 nm (**Fig. 1d**) which may reflect either (111) planes of the parent fcc Rh NPs or RhNi alloy NPs (Van der Waals radii of Rh and Ni are 200 pm and 163 pm respectively). Energy-dispersive X-ray spectroscopy (EDS) (**Fig. 1e, f** and **Fig. S7** and **S8**) evidenced local Rh:Ni atomic ratios of ~0.37 for individual NPs in $RhNi/Al_2O_3$ (GR), consistent with bulk elemental analysis (**Table 1**) and hence indicative of a uniform spatial distribution of both metals across the support. Unfortunately, it was not possible to obtain sub-nanometre resolution elemental maps due to electron beam damage. Metal loadings determined by inductively coupled plasma mass spectroscopy (ICP-MS) demonstrated that increasing the Rh^{3+} precursor concentration during the GR process increased the Rh loading from 0.22 wt% up to a maximum to 1.08 wt% (**Table S1**). The observation of a plateau beyond which additional Rh^{3+} precursor (**Fig. S9**) had no impact on the Rh loading suggests a self-limiting growth mode in which Rh is confined to a monolayer at the surface of Ni nanoparticles (consistent with the core-shell structure in **Scheme 1**). Rh incorporation is accompanied by a significant decrease in the Ni content, as expected for galvanic replacement in which Rh^{3+} ions exchange for metallic Ni atoms. Note that quantitative galvanic replacement of Ni^{2+} by Rh^{3+} should result in the introduction of ~0.4 wt% Rh, lower than the 1.08 wt% Rh observed. This indicates that although a significant proportion of Rh does exchange for Ni, some Rh deposits directly on the alumina support, or as multilayer islands on Rh encapsulated Ni nanoparticles. In contrast, chemical reduction resulted in a similar Rh content (0.91 wt%) as for galvanic replacement, but with minimal loss of Ni consistent with a pure deposition process.

Powder X-ray diffraction (XRD) patterns of Rh/Al_2O_3, Ni/Al_2O_3, $RhNi/Al_2O_3$ (CR), and $RhNi/Al_2O_3$ (GR) only exhibited reflections associated with the γ-Al_2O_3 support (JCPDS PDF 01-075-1862) and fcc Ni NPs (JCPDS PDF 00-045-1027) (**Fig. 1g**); the absence of reflections associated with any Rh phase is likely a consequence of the low Rh loadings (~1 wt%) and/or high Rh dispersion (although weak Rh reflections could be obscured by overlap with those from the alumina support). Closer examination of the (012) Ni reflection in the range 2θ = 56-59° reveals a small shift to lower angle for $RhNi/Al_2O_3$ (GR) and $RhNi/Al_2O_3$ (CR) compared to Ni/Al_2O_3 (**Fig. 1g inset**) indicative of very slight lattice expansions of only 0.4 % and 0.1 % respectively. These expansions are attributable to intermixing of only ~8-20 % of the available Rh

into Ni NPs, and hence inconsistent with bulk Rh-Ni alloying. Volume-averaged Ni NP sizes estimated by Scherrer analysis of the (110) reflection were between 2 and 3 nm (**Table 1**), being smallest for $RhNi/Al_2O_3$ (GR) as expected due to loss of Ni atoms during the GR process. The relative proportion of surface to total atoms (dispersion) in the 3 nm Ni NPs is ~40 %, and hence the direct exchange of Ni surface atoms by GR should result in a Rh:Ni molar ratio of 0.4,[28] in excellent agreement with that experimentally observed (**Table 1**) and consistent with the formation of a Rh monolayer decorating a Ni core.

Table 1 Metal content of Ni and Rh, bulk and surface Rh:Ni molar ratio, Rh loading, Ni particle size and BET surface area of the samples.

Catalyst	Metal content[a] wt%		Bulk Rh:Ni molar ratio[a]	Metal content[b] Atomic%	Surface Rh:Ni molar ratio[b]	Ni particle size[c] nm	BET surface area[d] $m^2.g^{-1}$
	Rh	Ni		Rh			
Ni/Al_2O_3	-	1.89	-		-	3.2	177
Rh/Al_2O_3	1.18	-	-	0.09	-	-	174
$RhNi/Al_2O_3$ (GR)	1.08	1.56	0.39	0.24	0.55	2.2	160
$RhNi/Al_2O_3$ (CR)	0.91	1.79	0.29	0.11	0.37	3.1	197

[a] Measured from ICP-MS.

[b] Measured from XPS.

[c] Calculated by Scherrer Equation using (110) of Ni in XRD result as reference.

[d] Measured by N_2 adsorption-desorption isotherm.

Rh 3d X-ray photoelectron spectroscopy (XPS) spectra of Rh/Al_2O_3 (after reduction at 400 °C for 1 h) exhibited two chemical environments assigned to metallic Rh and Rh^{3+} (in Rh_2O_3) [29] in an approximately 1:1 ratio with binding energies of 307.8 and 309.1 eV and full-width at half-maximum values of 2.5 and 3.2 eV respectively (**Fig. 1h**). Note that catalyst samples were air-exposed prior to XPS analysis and hence underwent partial re-oxidation. In contrast, only Rh^{3+} was observed for both $RhNi/Al_2O_3$ (CR) and $RhNi/Al_2O_3$ (GR), evidencing complete surface oxidation and hence a higher Rh dispersion than for Rh/Al_2O_3. There was no evidence of chemical shifts that might be anticipated from Rh-Ni alloying.[8] Surface Rh:Ni molar ratios for both bimetallic catalysts were higher than their bulk values (**Table 1**) indicative of (at least partial) Rh surface decoration of Ni NPs, with the $RhNi/Al_2O_3$ (GR) showing greater Rh surface enrichment than $RhNi/Al_2O_3$ (CR) consistent with a Ni@Rh core-shell structure for the former. Ni 2p XP spectra of the three catalysts (**Fig. S10**) reveal an essentially identical chemical environment for Ni/Al_2O_3, $RhNi/Al_2O_3$ (CR) and $RhNi/Al_2O_3$ (GR), comprising a spin-orbit split doublet at 586.7 eV and 874.1 characteristic of surface $Ni(OH)_2$ and satellites at 862.9 eV and

880.3 eV.[30] This is in accordance with our assignment of the chemical shift in the Rh 3p spectra of $RhNi/Al_2O_3$ (CR) and $RhNi/Al_2O_3$ (GR) as due to RhO_x formation and not Rh→Ni electron transfer.

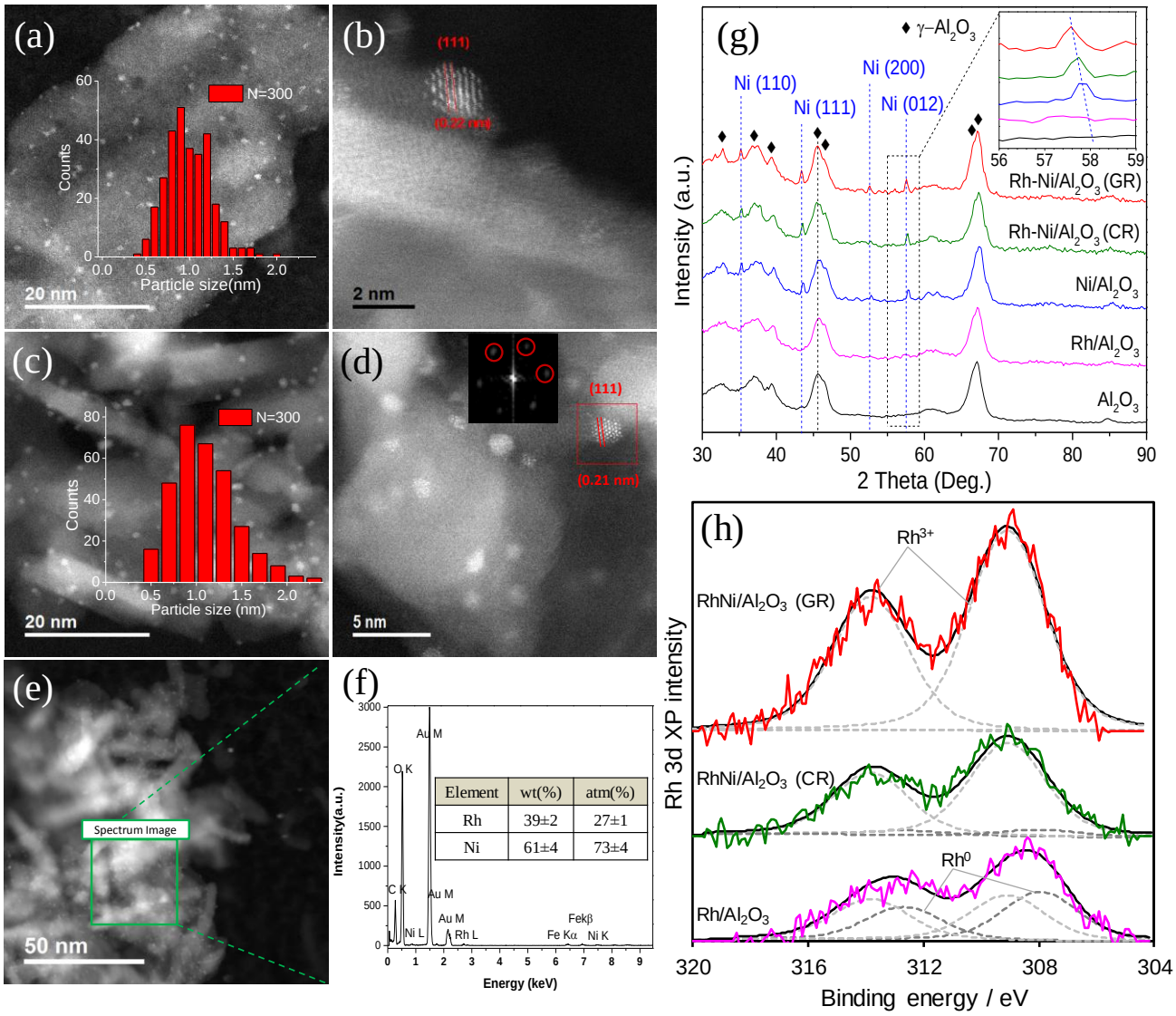

Fig. 1. HAADF-STEM images of (a, b) Rh/Al_2O_3 and (c-e) $RhNi/Al_2O_3$ (GR), (f) EDS elemental composition of $RhNi/Al_2O_3$ (GR) from image (e), (g) powder XRD patterns, and (h) fitted Rh 3d XP spectra.

Temperature-programmed reduction using hydrogen (H_2-TPR) was subsequently conducted to assess the reducibility of each samples (**Fig. 2a**). The principal reduction processes for Rh/Al_2O_3 and Ni/Al_2O_3 occur at 98 °C and 232 °C respectively, associated with the reduction of surface RhO_x[31] and NiO [32] to their metals. Higher temperature processes for Rh/Al_2O_3 (340 °C) and Ni/Al_2O_3 (two broad peaks above 500 °C) are attributed to the reduction of bulk Rh_2O_3 and Ni^{2+} species strongly interacting with the Al_2O_3 support (possibly present as $NiAl_2O_4$, reduction of which is a kinetically slow and stepwise process). H_2-TPR profiles of both bimetallic catalysts were similar, exhibiting strong peaks centred around 170 °C and 340 °C, but differed from either monometallic catalyst. The lower temperature peak for $RhNi/Al_2O_3$ (CR) was a broad composite of reduction processes associated with surface Rh_2O_3 (98 °C) and NiO (232 °C) present in spatially

separated Rh and Ni NPs, together with a new 170 °C feature which we attribute to the reduction of oxygen at the interface between Rh and Ni surface oxides, e.g. in core-shell RhNi NPs. For $RhNi/Al_2O_3$ (GR), only the latter (170 °C) peak was observed at low temperature, indicating that all the Rh in this catalyst was in intimate contact with Ni NPs, consistent with the Ni@Rh core-shell structure proposed above. The intensity of the high temperature (340 °C) peak was far greater in both bimetallics than for Rh/Al_2O_3, indicating either that proximity to Ni (or $NiAl_2O_4$) stabilises some Rh species towards reduction, and/or that Rh promotes Ni reduction by hydrogen spillover [33] (note the suppressed high temperature reduction features associated with $NiAl_2O_4$); in any event, the magnitude of this stabilisation is greatest for $RhNi/Al_2O_3$ (GR). Although the exact nature of this stabilisation is unclear, it may be associated with the slow and gradual reduction of strongly adsorbed Ni^{2+} species (e.g. $NiAl_2O_4$) [32] and concomitant diffusion and spillover of oxygen anions from nickel cores to interfacial RhO_x, analogous to that reported for Rh clusters and NPs on CeO_2.[34] The total H_2 consumption for $RhNi/Al_2O_3$ (GR) was ~2.5 times that of Rh/Al_2O_3, consistent with the higher degree of surface oxidation observed in the former by XPS, and double that of $RhNi/Al_2O_3$(CR) reflecting the higher dispersion of Ni@Rh core-shell NPs.

3.2. In-situ FTIR of CO chemisorption

CO chemisorption was also used to probe the surface composition of mono- and bimetallic catalysts after reduction in hydrogen at 400 °C by FTIR spectroscopy at low temperature (-196 °C) and low CO coverage (θ = 0.1 monolayers) to minimise coupling between neighbouring CO molecules (**Fig. 2b**). The major CO adsorption band at 2154-2158 cm^{-1} is attributed to weak binding to OH groups on the Al_2O_3 support in all cases.[35] Ni/Al_2O_3 exhibited an additional small, sharp band at 2172 cm^{-1} assigned to CO linearly bound to Ni^{2+}.[36] In contrast, Rh/Al_2O_3 exhibited a broad, strong band <2100 cm^{-1} characteristic of symmetric (2095 cm^{-1}) and asymmetric (2035 cm^{-1}) stretches of a $Rh^{\delta+}$-dicarbonyl complex and linearly bound CO on Rh metal (2065 cm^{-1}),[37] while a weak, broad band centred ~1864 cm^{-1} (**Fig. S11**) suggests the presence of bridging CO bound to Rh metal.[38] A small band at 2190 cm^{-1} may reflect CO adsorbed at Lewis acid Al^{3+} sites on alumina.[39] Both bimetallic catalysts also exhibit a weak band at 1775 cm^{-1} (**Fig. S11**), analogous to that reported for Rh-CO-Nb^{n+}[38] and related bimetallic systems [40, 41], and attributed to CO bridging neighbouring Rh and Ni atoms, evidencing an intimate bimetal interaction. $RhNi/Al_2O_3$ (CR) exhibited stronger Ni^{2+}-CO adsorption than $RhNi/Al_2O_3$ (GR), whereas $RhNi/Al_2O_3$ (GR) exhibited stronger Rh^{+}-CO adsorption, consistent with a higher dispersion of surface RhO_x species in the latter in agreement with H_2-TPR.

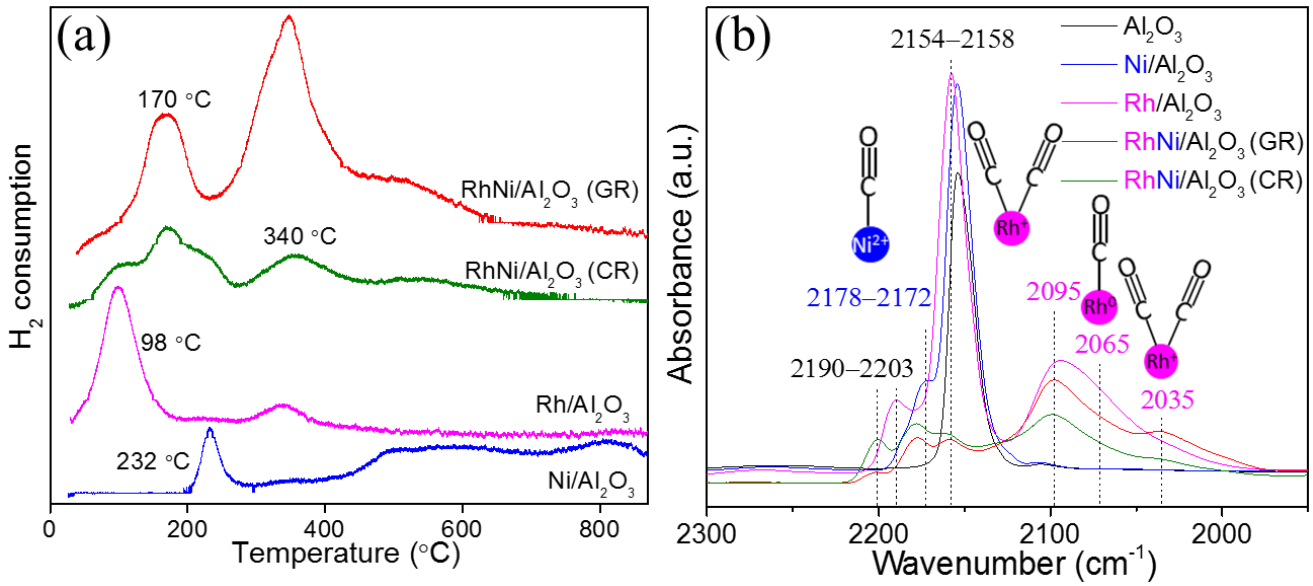

Fig. 2. (a) H_2 TPR profiles of Ni/Al_2O_3, Rh/Al_2O_3, $RhNi/Al_2O_3$ (GR) and $RhNi/Al_2O_3$ (CR), and (b) FTIR spectra following CO saturation and purging with 40 mbar He at -196 °C.

Rh K-edge X-ray absorption spectroscopy (XAS) analyses were performed on Rh/Al_2O_3, $RhNi/Al_2O_3$ (CR), and $RhNi/Al_2O_3$ (GR) after reduction treatment at 400 °C for 1h (**Fig. 3**). The normalised X-ray absorption near edge spectra (XANES) of all three catalysts are significantly different from metallic Rh but resemble literature spectra for Rh_2O_3,[42] indicating a high degree of oxidation. The energies and intensities of Rh/Al_2O_3 and $RhNi/Al_2O_3$ (CR) XANES features are superimposable, suggesting little difference in the average chemical environment of Rh within both catalysts. In contrast to the other two catalysts, the absorption edge in $RhNi/Al_2O_3$ (GR) was shifted to higher energy and the first post-edge feature ~23247 eV more clearly resolved into two distinct features; both indicative of a greater degree of Rh oxidation[43] in $RhNi/Al_2O_3$ (GR), consistent with XPS, H_2-TPR, and CO-FTIR. The local structural environment of Rh as determined by EXAFS was similar in all cases, being dominated by intense Rh-O scattering at 2.04 Å, and weaker Rh-Rh scattering ~3.09 Å, indicative of bulk Rh_2O_3.[44] However, the Rh-O nearest neighbour coordination number was highest for $RhNi/Al_2O_3$ (GR), approximating that observed in bulk Rh_2O_3, and in accordance with a fully oxidised Rh overlayer encompassing a Ni NP. Weak metal-metal scattering at ~2.65 Å confirms the presence of a Rh metal core for the Rh/Al_2O_3 and $RhNi/Al_2O_3$ (CR), but for $RhNi/Al_2O_3$ (GR) may also reflect Rh-Ni interactions, and indeed the Fourier transformed radial distribution function for $RhNi/Al_2O_3$ (GR) exhibits peak splitting between 2-3 Å which was best fitted by a superposition of Rh-Rh and Rh-Ni scatterers (R-factor = 2.4×10^{-4}). Observation of a Rh-Ni scattering shell provides direct evidence for intimate bimetal contact. Post-reaction, the $RhNi/Al_2O_3$ (GR) catalyst shows only a small change in the EXAFS, with Rh-O and Rh-Ni coordination numbers falling from 5.9 to 5 and 1.3 to 0.7 respectively, and the Rh-Rh coordination number rising from 1.2 to 1.7, indicating partial reduction of surface Rh_2O_3 occurs under the reducing environment employed. The small decrease in Rh-O and Rh-Ni coordination and concomitant emergence of weak Rh-Rh coordination suggests that the initial core-

shell structure is retained; the Rh local environment remains consistent with a truncated oxide overlayer interspersed with small Rh clusters.

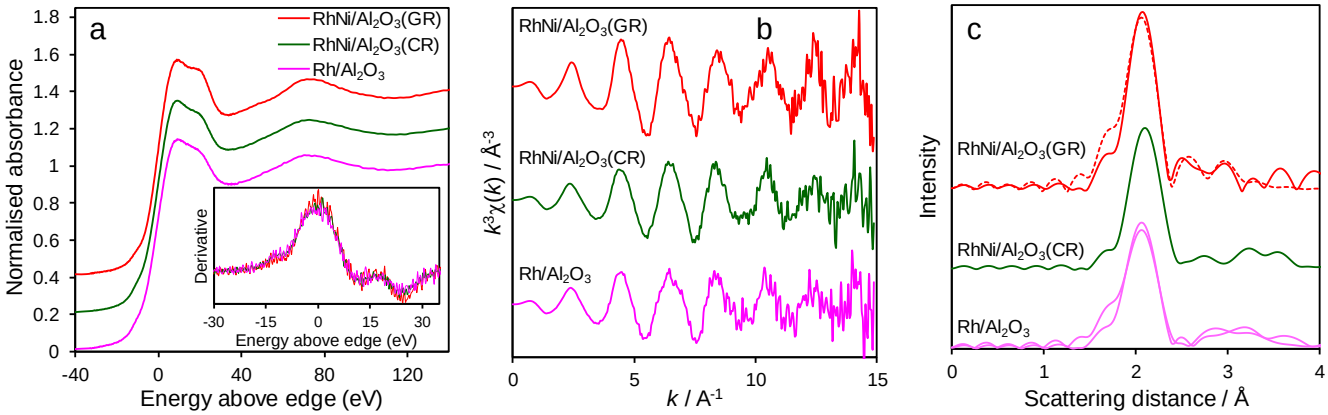

Fig. 3. Rh K-edge XAS spectra for Rh/Al_2O_3 (green), $RhNi/Al_2O_3$ (CR) (red) and $RhNi/Al_2O_3$ (GR) (blue) catalysts: (a) edge-step normalised XANES spectra; (b) corresponding background subtracted k^3-weighted EXAFS signal $\chi(k)$; and (c) corresponding k^3-weighted Fourier transform magnitudes.

Table 2. Rh K-edge EXAFS fitting results of Rh/Al_2O_3, fresh and used $RhNi/Al_2O_3$ (GR) catalysts (see Supporting Information for fit comparison; fit variables indicated with bracketed standard deviation).

Sample	**Absorber-backscatter**	**Coordination number**	**R (Å)**[a]	**σ^2 (Å^2)**[b]
	Rh – O	4.5	2.04(1)	0.004(1)
*Rh/Al_2O_3	Rh – Rh	0.8	2.70(3)	0.008(2)
	Rh – Rh	0.2	3.09(3)	0.001(3)
**Fresh $RhNi/Al_2O_3$ (GR)	Rh – O	5.9	2.04(1)	0.003(1)
	Rh – Rh	1.2	2.63(2)	0.002(2)
	Rh – Ni	1.3	2.63(3)	0.003(3)
*** Post-reaction $RhNi/Al_2O_3$ (GR)	Rh – O	5	2.05(1)	0.005(1)
	Rh – Rh	1.7	2.67(5)	0.009(5)
	Rh – Ni	0.7	2.63(6)	0.005(5)
	Rh – Rh	0.5	3.13(4)	0.006(3)

S_{02} = 0.85(Set) Fitting k-weight = 3; Fitting window = Kaiser-Bessel; Fitting Space = R.

* R-factor = $7.6x10^{-4}$; E_0 = 2(2); k-range = 2 – 13; R-range = 1.3 – 3.5.

** R-factor = $2.4x10^{-4}$; E_0 = 1(2); k-range = 2 – 13; R-range = 1.3 – 3.

*** R-factor = $5.9x10^{-4}$; E_0 = 1(2); k-range = 2 – 13; R-range = 1.3 – 3.5.

[a] Interatomic scattering distance.

[b] Debye-Waller factor.

The preceding surface and bulk structural characterisation present a consistent picture wherein the $RhNi/Al_2O_3$ (GR) catalyst comprises highly dispersed (~1 nm) Ni nanoparticles encapsulating by a RhO_x monolayer, whereas $RhNi/Al_2O_3$ (CR) comprises larger (≥1.3 nm) RhNi bulk alloy nanoparticles. A significant proportion of Rh atoms in Rh/Al_2O_3 and $RhNi/Al_2O_3$ (CR) reside subsurface in a metallic state and hence are not anticipated to participate in catalytic CO_2 methanation.

3.3. CO_2 methanation performance

CO_2 methanation was subsequently compared over the mono- and bimetallic catalysts, which were >90 % selective to CH_4 versus CO (**Fig. S14**) but exhibited significant differences in CO_2 light-off (**Fig. 4a**). For $RhNi/Al_2O_3$ (GR), the carbon mass balance was >99 %. Activity decreased in the order $RhNi/Al_2O_3$ (GR) > Rh/Al_2O_3 > $RhNi/Al_2O_3$ (CR) > Ni/Al_2O_3, evidencing a strong Rh-Ni synergy for $RhNi/Al_2O_3$ (GR). The similar reactivity of Rh/Al_2O_3 and $RhNi/Al_2O_3$ (GR) is consistent with a core-shell model (rather than a bulk or surface alloy) for the latter in which the principal role of Ni is to increase the Rh dispersion. The effect of Rh precursor concentration on CO_2 methanation activity is investigated, and the activity increases in the order RhNi GR-1 < RhNi GR-4 < RhNi GR-2 < RhNi GR-3 (**Fig. S15**). This is because of a self-limiting growth mode in which Rh is confined to a monolayer at the surface of Ni nanoparticles and further increase of Rh^{3+} precursor had no impact on the Rh loading (consistent with the core-shell structure) (**Table S1**). The specific CH_4 productivities (**Fig. 4b**) reveal an almost two-fold rate-enhancement for versus Rh/Al_2O_3 at 250 °C, despite both containing the same amount of Rh, while Ni/Al_2O_3 is almost inactive at this temperature. These results suggest that the smaller Ni particle size and higher Rh dispersion of $RhNi/Al_2O_3$ (GR) promote methanation. Apparent activation energies from a leading edge analysis at low conversion reveal similar values for core-shell $RhNi/Al_2O_3$ (GR) and Rh/Al_2O_3 catalysts of 66±5 and 70±5 $kJ.mol^{-1}$ respectively, indicating a common reaction mechanism. In contrast, the apparent activation energy for $RhNi/Al_2O_3$ (CR) catalyst was 96±5 $kJ.mol^{-1}$, reflecting the co-existence of highly active Rh with relatively inactive Ni surface atoms. The lower activity of $RhNi/Al_2O_3$ (CR) versus Rh/Al_2O_3 appears to simply reflect the lower number of surface Rh atoms, and larger mean size (and broader distribution) of NPs (**Fig. S6**) in the former. Lifetime tests of $RhNi/Al_2O_3$ (GR) at 250 °C demonstrate excellent stability (**Fig. S16**) with CO_2 conversion remaining constant ~70 % for 25 h on-stream. Future studies will investigate accelerated ageing at higher reaction temperature (>500 °C) and extended lifetime testing over hundreds of hours at lower conversion (<50 %).[45] Future studies HAADF-STEM imaging of $RhNi/Al_2O_3$ (GR) post-reaction reveals negligible particle sintering (**Fig. S17**) confirming that Ni@Rh core-shell nanoparticles formed by galvanic replacement are stable on-stream. Fair assessment of the intrinsic activity of different Rh catalysts requires a quantitative comparison of their turnover frequencies (TOFs) per surface Rh site; Ni is essentially inert at 250 °C and hence is omitted from these calculations. Corresponding TOFs per surface Rh for $RhNi/Al_2O_3$ (GR) are more than double those of literature catalysts (**Table S2**) at a comparable reaction temperature, which we attribute to the high

dispersion of catalytically active Rh sites and their stabilisation against sintering and/or reduction. The RhNi/Al_2O_3 (GR) TOF is similar to that of Rh/Al_2O_3 indicative of a common active site, consistent with both catalysts comprising entirely Rh terminated surfaces. Although the RhNi/Al_2O_3 (CR) TOF is higher than that for RhNi/Al_2O_3 (GR) and Rh/Al_2O_3, this is likely an overestimate reflecting the implicit assumption that only surface Rh atoms contribute to CO_2 methanation in RhNi alloy nanoparticles.

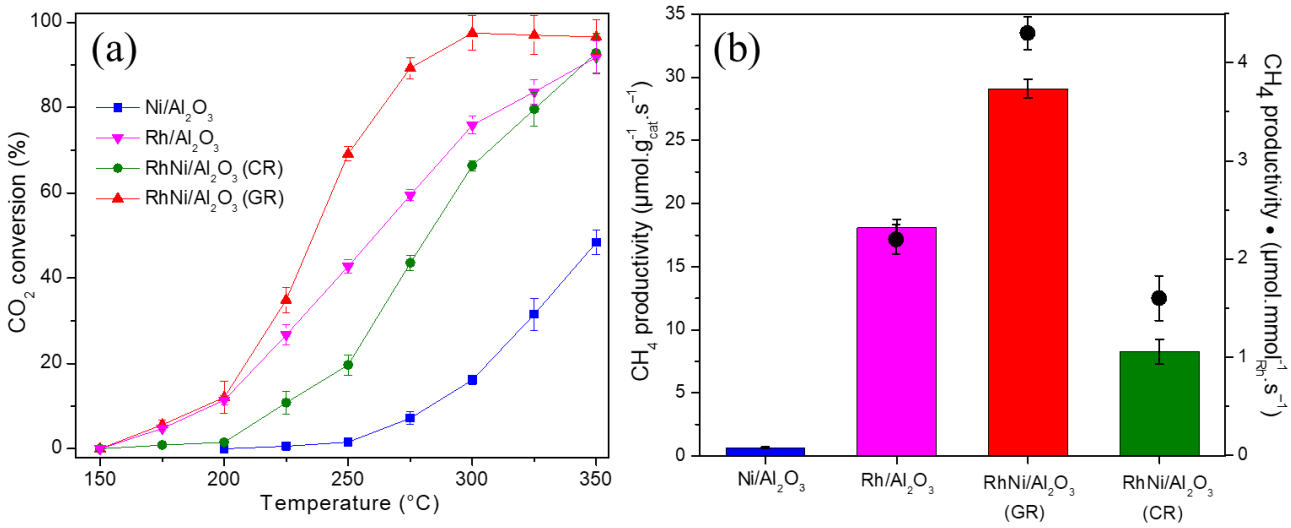

Fig. 4. Catalytic activity of Ni/Al_2O_3, Rh/Al_2O_3, RhNi/Al_2O_3 (CR), and RhNi/Al_2O_3 (GR) for CO_2 methanation: (a) CO_2 conversion versus reaction temperature; (b) Rh normalised CH_4 productivity at 250 °C.

3.4. In situ CO_2 Methanation

The nature of surface species present during CO_2 methanation over Ni/Al_2O_3, Rh/Al_2O_3, and RhNi/Al_2O_3 (GR) catalysts was subsequently investigated by in-situ DRIFTS (**Fig. 5** and **Fig. S18**). In all cases, absorption bands at 1651 (1656, 1657) (υ_{as}), 1444 (1437, 1436) (υ_s), 1229(γ_{OH}), and 3623/3600 cm^{-1} (γ_{OH}) are assigned to adsorbed bicarbonates (HCO_3) associated with hydroxyls on Al_2O_3 (**Fig. 5a-c**).[22] Bands at 1592 (1593) (υ_{as}), 1392 (1393) (δ_{CH}), and 1372 (1373, 1376) cm^{-1} (υ_s) (**Fig. 5a-c**) and 2905 (2906) (υ_{CH}) (**Fig. 5d** and **Fig. S18**) are characteristic of monodentate formate (type I) bound to the alumina support,[46] while a new band at 3000 (2998, 3001) cm^{-1} (**Fig. 5d**) emerging at 150 °C is assigned to the C-H stretch of bidentate formate (type II). The υ(COO) bands of type I and type II formate overlap and are hence difficult to distinguish.[47] Bands at 2033 cm^{-1} (shifting to 2010 cm^{-1} at higher temperature) and 1843 (1840) cm^{-1} for RhNi/Al_2O_3 (GR) (**Fig. 5c**) and Rh/Al_2O_3 (**Fig. 5e**) are associated with C-O stretches of linear and bridging CO respectively bound to metallic Rh, while that at 1724 cm^{-1} (**Fig. 5c** and **Fig. 5e** insets), present between 50 and 150 °C, is attributed to formyl (HCO) formation; note that neither reactively-formed CO nor formyl were observed over Ni/Al_2O_3 (**Fig. 5b**) or the Al_2O_3 support (**Fig. 5a**). Gas phase methane was observed at 3015 (3016) (**Fig. 5d** and **Fig. S18a-c**) and 1305 cm^{-1} (**Fig. 5 b-c, Fig. 5e**) over the metal catalysts >250 °C. The observation of reactively-formed CO over Rh/Al_2O_3 and RhNi/Al_2O_3 (GR)

catalysts shows that Rh (but not Ni) is active for the dissociative chemisorption of CO_2 at room temperature. Room temperature formate production from bicarbonate on the alumina was only observed in the presence of Rh (**Fig. 5c** and **Fig. 5e**), consistent with the latter's high activity for hydrogen dissociation, and indicating a hydrogen spillover mechanism between metal and support.[33] Quantitative comparison of the surface intermediates over Rh/Al_2O_3 and $RhNi/Al_2O_3$ (GR) reveals a similar formate concentration and temperature profile (unsurprising since this is associated with the common support), but a higher concentration of reactively-formed CO over the monometallic catalyst (also expected since this contains more Rh).

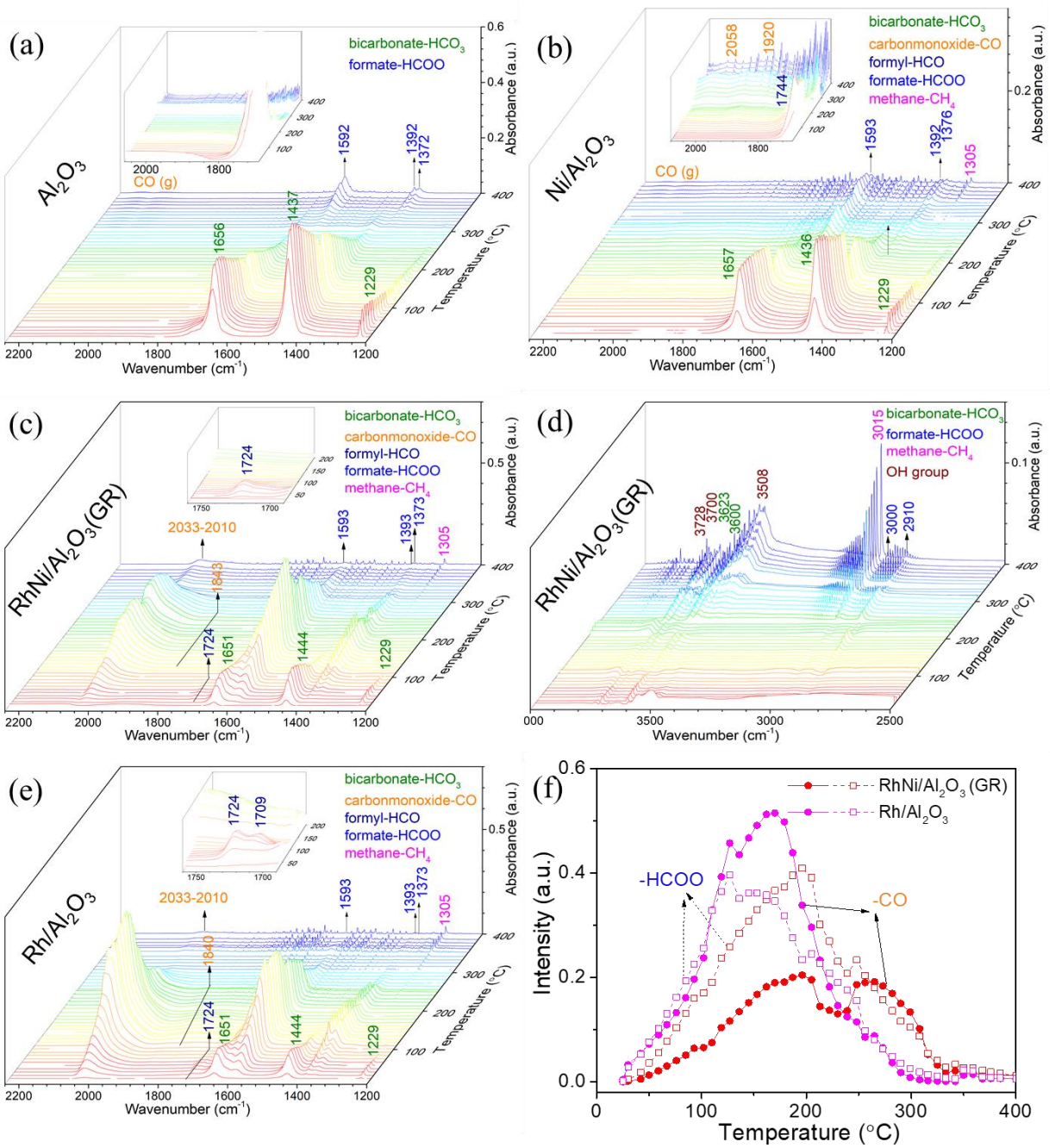

Fig. 5. In-situ DRIFTS spectra of CO_2 methanation over (a) Al_2O_3, (b) Ni/Al_2O_3, (c-d) $RhNi/Al_2O_3$ (GR), and (e) Rh/Al_2O_3 for CO_2 methanation from 30-400 °C, and (f) corresponding temperature dependent CO (2033-2010 cm^{-1}) and formate (1593 cm^{-1}) intensities over Rh/Al_2O_3 and $RhNi/Al_2O_3$ (GR) (CO_2:H_2:Ar=2:8:30, 40 mL/min total).

Note that in-situ observation of CO bound to metallic Rh during CO_2 methanation is not inconsistent with XPS, XAS and CO FTIR results for the as-prepared $RhNi/Al_2O_3$ (GR) catalyst in which the majority of surface Rh is oxidised. H_2-TPR (**Fig. 2a**) show that RhO_x species are heavily reduced >200 °C, and hence metallic surface Rh is expected to form at 250 °C under the net reducing conditions encountered during CO_2 methanation, as evidenced by post-reaction XAS (**Table 2**). Oxidised Rh present in the $RhNi/Al_2O_3$ (GR) surface undergoes (at least partial) in-situ reduction during CO_2 methanation.

Further insight into the reaction mechanism was obtained by separately introducing the CO_2 and hydrogen. CO_2 was first introduced to as-prepared (hydrogen-free) $RhNi/Al_2O_3$ (GR) and Rh/Al_2O_3 catalysts at 30 °C for 20 min, sufficient for the DRIFTS spectra to reach steady-state (**Fig. 6a-b**). In both cases, a similar concentration of surface bicarbonate was immediately formed, associated with hydroxyls over the Al_2O_3 support. Reactively-formed CO was also observed over both catalysts (bands at 2093 and 2030 cm^{-1} attributed to Rh^+-CO as a dicarbonyl complex, and that at 2064 cm^{-1} due to CO linearly bound to Rh^0), arising from the dissociative adsorption of CO_2 over Rh sites at room temperature; low temperature CO_2 dissociation to CO is previously reported for Cu/TiO_{2-x} at 25 °C [48] and Rh/Al_2O_3 at 125 °C.[12] Only the Rh^+-CO band remained on heating to 250 °C and purging with Ar (**Fig. 6c**), consistent with reports that Rh(I) dicarbonyl is stable <300 °C over Al_2O_3 ultrathin films,[49] and coincident with loss of the bicarbonate bands presumably due to decomposition back to gaseous CO_2. Subsequent introduction of H_2 resulted in the immediate loss of the remaining chemisorbed CO over the $RhNi/Al_2O_3$ (GR) catalyst and concomitant evolution of reactively-formed CH_4 (**Fig. 6c**); this is strong evidence that CO (on Rh) is the critical intermediate for CH_4 production. Similar behaviour was observed over the Rh/Al_2O_3 catalyst, although a small concentration of unreacted CO remained after H_2 addition, which may account for the lower reactivity of the monometallic system (presumably arising from site-blocking). Surprisingly, H_2 addition was also accompanied by the appearance of trace surface formate, whose origin is not yet clear. The relative reactivity of CO and formate towards H_2 was subsequently investigated by introducing CO_2 to a freshly reduced catalyst (which still possessed trace surface hydrogen) at 30 °C for 20 min to seed the surface with CO and formate prior to heating to 250 °C, purging with Ar, and the introduction of H_2 (**Fig. 6d**). The results were striking; as before, chemisorbed CO was immediately consumed following H_2 addition coincident with the evolution of CH_4, whereas surface formate remained constant. This is strong evidence that CH_4 is formed from reactively-formed CO and not formate.

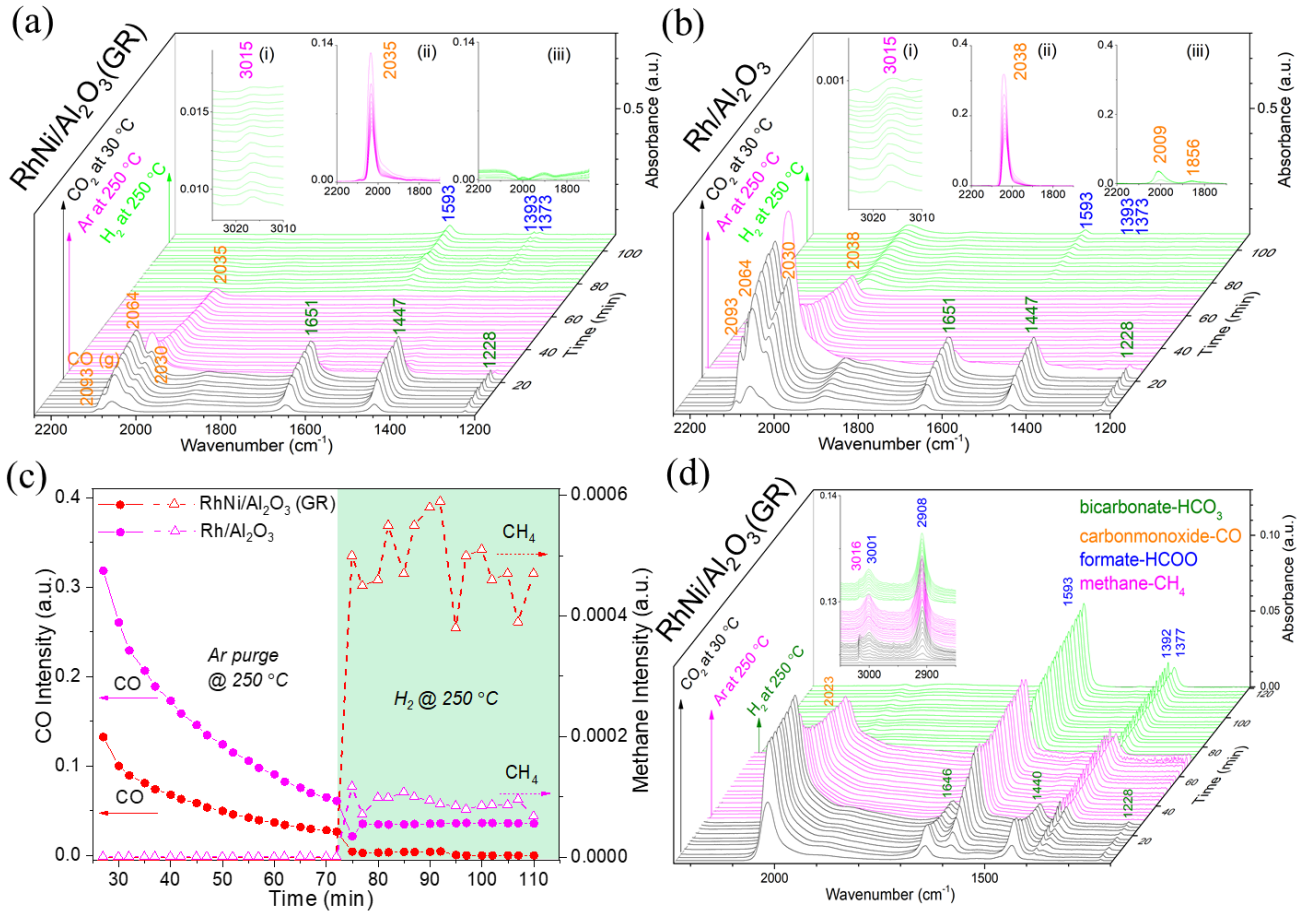

Fig. 6. In situ DRIFTS spectra during CO_2 adsorption and reaction over (a) $RhNi/Al_2O_3$ (GR) and (b) Rh/Al_2O_3: inset (i) shows CH_4 formation in H_2 at 250 °C, and (ii-iii) adsorbed and reacting CO under Ar and H_2 at 250 °C respectively. (c) Corresponding peak CO (2035 cm^{-1}) and CH_4 (3015 cm^{-1}) peak intensities for Rh/Al_2O_3 and $RhNi/Al_2O_3$ (GR) during purging and H_2 admission, and (d) CO_2 adsorption and over pre-reduced $RhNi/Al_2O_3$ (GR) containing residual surface hydrogen.

3.5. Proposed Reaction Pathways for CO_2 Methanation on $RhNi/Al_2O_3$

Proposed reaction pathways for CO_2 methanation over Rh catalysts are illustrated in **Scheme 2** and highlight possible contributions from metal and support. Bicarbonate is formed by the reaction of CO_2 and hydroxide groups on the alumina at room temperature (step 1'), and can in turn react to generate surface formate in the presence of atomic hydrogen (generated at metal nanoparticles) (step 2'). However, subsequent hydrogenation of formate (steps 3'-5') is extremely slow over both mono- and bimetallic Rh catalysts at catalytically relevant temperature (250 °C), and hence formate appears to be a spectator in CO_2 methanation.[24, 29] CO_2 and hydrogen both dissociatively chemisorb over Rh at room temperature, and reacts >200 °C to form methane through hydrogenation of reactively-formed CO (step 2) and the resulting formyl surface intermediate (step 3). It is interesting to note that Swalus et al[18] required a physical mixture of Ni/activated carbon and $Rh/\gamma\text{-}Al_2O_3$ catalyst to achieve efficient CO_2 methanation, proposing that H_2

activation was confined to the Ni catalyst whereas CO_2 dissociation occurred over the Rh component. Our work demonstrates that Rh alone can activate both reactants, and that the primary role of Ni is to improve the dispersion (utilisation) of the active Rh component through a core-shell nanostructure; separating (or alloying) Rh and Ni over the same support as in $RhNi/Al_2O_3$ (CR) produces a less active catalyst.

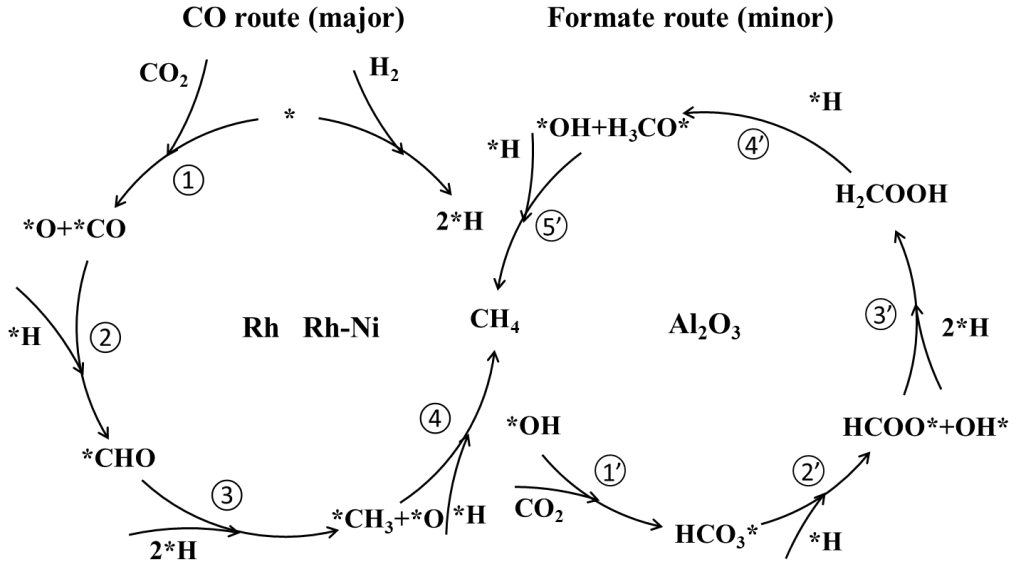

Scheme 2. Proposed parallel pathway reaction mechanism for CO_2 methanation reaction on $RhNi/Al_2O_3$ (GR) catalyst. The asterisk represents the adsorption site for the intermediate species.

4. Conclusions

Galvanic replacement (GR) provides a simple, low temperature synthetic route to induce a strong metal-metal interaction in bimetallic RhNi catalysts. Physicochemical characterisation by electron microscopy, XRD, XPS, TPR, and porosimetry demonstrates the retention of small (1-2 nm) metallic Ni nanoparticles present in the parent Ni/Al_2O_3 following either GR or a conventional chemical reduction (CR) treatment with $RhCl_3$. There is no evidence for significant Rh-Ni intermixing in the resulting $RhNi/Al_2O_3$ (GR) catalyst. XAS, XPS, and in-situ IR of CO chemisorbed at low temperature indicate the $RhNi/Al_2O_3$ (GR) catalyst comprises predominantly Rh^{3+} dispersed as an oxide shell encapsulating a Ni core, whereas the $RhNi/Al_2O_3$ (CR) catalyst is an inhomogeneous mix of Rh and RhNi alloy nanoparticles. Dispersing Rh over Ni nanoparticles in the $RhNi/Al_2O_3$ (GR) catalyst doubles methane productivity from CO_2 at 250 °C and improves high temperature methane selectivity, relative to Rh/Al_2O_3. In contrast, the conventionally prepared $RhNi/Al_2O_3$ (CR) catalyst is less active than either $RhNi/Al_2O_3$ (GR) or Rh/Al_2O_3, albeit superior to Ni/Al_2O_3 which is almost inactive <300 °C. Operando IR spectroscopy reveals two competing reaction pathways for CO_2 over both $RhNi/Al_2O_3$ (GR) and Rh/Al_2O_3, both involving room temperature CO_2 dissociative adsorption: the first involves the alumina support, and occurs through the reaction of CO_2 with surface hydroxyls to form bicarbonate, which is subsequently reduced to a formate surface spectator by atomic hydrogen spilled over from Rh; the second, occurs over Rh sites, with the

resultant reactively-formed CO emerging as the critical catalytic intermediate that undergoes hydrogenation to CH_4 >200 °C. In summary, Ni@Rh core-shell catalysts wherein Rh atoms are highly dispersed, offer high activity and selectivity for CO_2 methanation with productivities four times faster than achievable by chemical reduction or exsolution synthesis of RhNi bimetallic alloys; Rh dispersed over Ni nanoparticles is superior to Rh alloyed with Ni. Extending the GR method to more dilute (Rh poor) bimetallic $RhNi/Al_2O_3$ (GR) catalysts further increases the specific activity (per noble metal atom), consistent with recent reports that Rh nanoclusters,[50] but not isolated atoms or large nanoparticles, are extremely active and selective for CO_2 reduction to methane.[16] It is anticipated that the galvanic replacement strategy can be extended to the fabrication of other heterogeneous bimetallic catalysts to deliver improved, and tunable performance and encourage precious metal thrifting.

Author Contribution

Y.W. and H.A. performed catalyst synthesis, characterisation and activity testing. S.B. A.L. and K.W. conducted XAS experiments at the Australian Synchrotron. A.T. and R.S. supported in situ DRIFTS experiments at the Fritz-Haber-Institut der Max-Planck-Gesellschaft. J.S., T.M., A.T., R.S., A.L., K.W., and R.A. provided technical and scientific support as well as played a supervisory role in the research. The manuscript was prepared by Y.W., H.A., S.B., and H.S and revised by all the authors.

Declaration of Competing Interest

The authors declare that they have no known competing financial interests or personal relationships that could have appeared to influence the work reported in this paper.

Acknowledgments

Yuan Wang thanks the German Academic Exchange Service (DAAD) and Australian Nanotechnology Network for financial support. Danail Ivanov and Thomas Lunkenbein are thanked for their help with HAADF-STEM imaging. The authors acknowledge Jutta Kröhnert, Dr. Friedrich Seitz, Daniel Brennecke, Dr. Andrey Tarasov, Marie-M. Millet and Dr. Yuanqing Wang from the Fritz Haber Institute. Hamidreza Arandiyan acknowledges financial support through the University of Sydney Research Fellowship (G197582) program.

Supporting Information

Additional details on catalyst characterisation and reactivity are provided.

References

[1] J.K. Nørskov, T. Bligaard, B. Hvolbæk, F. Abild-Pedersen, I. Chorkendorff, C.H. Christensen, The nature of the active site in heterogeneous metal catalysis, Chem. Soc. Rev., 37 (2008) 2163-2171.
[2] C. Leclercq, S. Pietrzyk, L. Gengembre, L. Leclercq, Bimetallic Ni-Rh catalysts: I surface composition and chemisorption properties, Appl. Catal., 27 (1986) 299-312.
[3] W. Luo, M. Sankar, A.M. Beale, Q. He, C.J. Kiely, P.C.A. Bruijnincx, B.M. Weckhuysen, High performing and stable supported nano-alloys for the catalytic hydrogenation of levulinic acid to γ-valerolactone, Nat. Commun., 6 (2015) 6540.
[4] A.F. Lee, C.J. Baddeley, C. Hardacre, R.M. Ormerod, R.M. Lambert, G. Schmid, H. West, Structural and Catalytic Properties of Novel Au/Pd Bimetallic Colloid Particles: EXAFS, XRD, and Acetylene Coupling, J. Phys. Chem., 99 (1995) 6096-6102.
[5] Z. Yin, Y. Zhang, K. Chen, J. Li, W. Li, P. Tang, H. Zhao, Q. Zhu, X. Bao, D. Ma, Monodispersed bimetallic PdAg nanoparticles with twinned structures: Formation and enhancement for the methanol oxidation, Sci. Rep., 4 (2014) 4288.
[6] Y. Wang, H. Arandiyan, J. Scott, M. Akia, H. Dai, J. Deng, K.-F. Aguey-Zinsou, R. Amal, High Performance Au–Pd Supported on 3D Hybrid Strontium-Substituted Lanthanum Manganite Perovskite Catalyst for Methane Combustion, ACS Catal., 6 (2016) 6935-6947.
[7] S. Xie, Y. Liu, J. Deng, X. Zhao, J. Yang, K. Zhang, Z. Han, H. Arandiyan, H. Dai, Effect of transition metal doping on the catalytic performance of Au–Pd/3DOM Mn2O3 for the oxidation of methane and o-xylene, Appl. Catal. B, 206 (2017) 221-232.
[8] J. Zhang, J. Teo, X. Chen, H. Asakura, T. Tanaka, K. Teramura, N. Yan, A Series of NiM (M = Ru, Rh, and Pd) Bimetallic Catalysts for Effective Lignin Hydrogenolysis in Water, ACS Catal., 4 (2014) 1574-1583.
[9] Y. Kang, Q. Xue, R. Peng, P. Jin, J. Zeng, J. Jiang, Y. Chen, Bimetallic AuRh nanodendrites consisting of Au icosahedron cores and atomically ultrathin Rh nanoplate shells: synthesis and light-enhanced catalytic activity, Npg Asia Mater., 9 (2017) e407.
[10] M. Thema, F. Bauer, M. Sterner, Power-to-Gas: Electrolysis and methanation status review, Renew. Sust. Energ. Rev., 112 (2019) 775-787.
[11] W. Li, H. Wang, X. Jiang, J. Zhu, Z. Liu, X. Guo, C. Song, A short review of recent advances in CO2 hydrogenation to hydrocarbons over heterogeneous catalysts, RSC Adv., 8 (2018) 7651-7669.
[12] A. Beuls, C. Swalus, M. Jacquemin, G. Heyen, A. Karelovic, P. Ruiz, Methanation of CO2: Further insight into the mechanism over Rh/γ-Al2O3 catalyst, Appl. Catal. B, 113-114 (2012) 2-10.
[13] K. Ray, G. Deo, A potential descriptor for the CO2 hydrogenation to CH4 over Al2O3 supported Ni and Ni-based alloy catalysts, Appl. Catal. B, 218 (2017) 525-537.
[14] M. Younas, L. Loong Kong, M.J.K. Bashir, H. Nadeem, A. Shehzad, S. Sethupathi, Recent Advancements, Fundamental Challenges, and Opportunities in Catalytic Methanation of CO2, Energ. Fuel, 30 (2016) 8815-8831.
[15] H. Arandiyan, Y. Wang, J. Scott, S. Mesgari, H. Dai, R. Amal, In Situ Exsolution of Bimetallic Rh–Ni Nanoalloys: a Highly Efficient Catalyst for CO2 Methanation, ACS Appl. Mater. Interfaces, 10 (2018) 16352-16357.
[16] J.C. Matsubu, V.N. Yang, P. Christopher, Isolated Metal Active Site Concentration and Stability Control Catalytic CO2 Reduction Selectivity, J. Am. Chem. Soc., 137 (2015) 3076-3084.
[17] D. Heyl, U. Rodemerck, U. Bentrup, Mechanistic Study of Low-Temperature CO2 Hydrogenation over Modified Rh/Al2O3 Catalysts, ACS Catal., 6 (2016) 6275-6284.
[18] C. Swalus, M. Jacquemin, C. Poleunis, P. Bertrand, P. Ruiz, CO2 methanation on Rh/γ-Al2O3 catalyst at low temperature: “In situ” supply of hydrogen by Ni/activated carbon catalyst, Appl. Catal. B, 125 (2012) 41-50.
[19] B. Yan, Q. Wu, J. Cen, J. Timoshenko, A.I. Frenkel, D. Su, X. Chen, J.B. Parise, E. Stach, A. Orlov, J.G. Chen, Highly active subnanometer Rh clusters derived from Rh-doped SrTiO3 for CO2 reduction, Appl. Catal. B, 237 (2018) 1003-1011.
[20] B. Miao, S.S.K. Ma, X. Wang, H. Su, S.H. Chan, Catalysis mechanisms of CO2 and CO methanation, Catal. Sci. Technol., 6 (2016) 4048-4058.
[21] L. Falbo, C.G. Visconti, L. Lietti, J. Szanyi, The effect of CO on CO2 methanation over Ru/Al2O3 catalysts: a combined steady-state reactivity and transient DRIFT spectroscopy study, Appl. Catal. B, 256 (2019) 117791.

[22] X. Wang, H. Shi, J.H. Kwak, J. Szanyi, Mechanism of CO2 Hydrogenation on Pd/Al2O3 Catalysts: Kinetics and Transient DRIFTS-MS Studies, ACS Catal., 5 (2015) 6337-6349.
[23] Q. Pan, J. Peng, S. Wang, S. Wang, In situ FTIR spectroscopic study of the CO2 methanation mechanism on Ni/Ce0.5Zr0.5O2, Catal. Sci. Technol., 4 (2014) 502-509.
[24] A. Karelovic, P. Ruiz, Mechanistic study of low temperature CO2 methanation over Rh/TiO2 catalysts, J. Catal., 301 (2013) 141-153.
[25] M. Marwood, R. Doepper, A. Renken, In-situ surface and gas phase analysis for kinetic studies under transient conditions The catalytic hydrogenation of CO2, Appl. Catal. A, 151 (1997) 223-246.
[26] X. Li, H. Dai, J. Deng, Y. Liu, S. Xie, Z. Zhao, Y. Wang, G. Guo, H. Arandiyan, Au/3DOM LaCoO3: High-performance catalysts for the oxidation of carbon monoxide and toluene, Chem. Eng. J., 228 (2013) 965-975.
[27] X. Lu, J. Chen, S.E. Skrabalak, Y. Xia, Galvanic replacement reaction: A simple and powerful route to hollow and porous metal nanostructures, Proceedings of the Institution of Mechanical Engineers, Part N: Journal of Nanoengineering and Nanosystems, 221 (2007) 1-16.
[28] A. Borodziński, M. Bonarowska, Relation between Crystallite Size and Dispersion on Supported Metal Catalysts, Langmuir, 13 (1997) 5613-5620.
[29] A. Karelovic, P. Ruiz, CO2 hydrogenation at low temperature over Rh/γ-Al2O3 catalysts: Effect of the metal particle size on catalytic performances and reaction mechanism, Appl. Catal. B, 113–114 (2012) 237-249.
[30] NIST X-ray Photoelectron Spectroscopy Database, Version 4.1, (National Institute of Standards and Technology, Gaithersburg, 2012.
[31] M. Piumetti, M. Hussain, D. Fino, N. Russo, Mesoporous silica supported Rh catalysts for high concentration N2O decomposition, Appl. Catal. B, 165 (2015) 158-168.
[32] X. Zhao, G. Lu, Modulating and controlling active species dispersion over Ni–Co bimetallic catalysts for enhancement of hydrogen production of ethanol steam reforming, Int. J. Hydrogen Energ., 41 (2016) 3349-3362.
[33] L. Qian, W. Cai, L. Zhang, L. Ye, J. Li, M. Tang, B. Yue, H. He, The promotion effect of hydrogen spillover on CH4 reforming with CO2 over Rh/MCF catalysts, Appl. Catal. B, 164 (2015) 168-175.
[34] H. Cordatos, T. Bunluesin, J. Stubenrauch, J.M. Vohs, R.J. Gorte, Effect of ceria structure on oxygen migration for Rh/ceria catalysts, J. Phys. Chem., 100 (1996) 785-789.
[35] K. Hadjiivanov, J. Lamotte, J.-C. Lavalley, FTIR Study of Low-Temperature CO Adsorption on Pure and Ammonia-Precovered TiO2 (Anatase), Langmuir, 13 (1997) 3374-3381.
[36] K. Mette, S. Kühl, A. Tarasov, M.G. Willinger, J. Kröhnert, S. Wrabetz, A. Trunschke, M. Scherzer, F. Girgsdies, H. Düdder, K. Kähler, K.F. Ortega, M. Muhler, R. Schlögl, M. Behrens, T. Lunkenbein, High-Temperature Stable Ni Nanoparticles for the Dry Reforming of Methane, ACS Catal., 6 (2016) 7238-7248.
[37] S. Trautmann, M. Baerns, Infrared Spectroscopic Studies of CO Adsorption on Rhodium Supported by SiO2, Al2O3, and TiO2, J. Catal., 150 (1994) 335-344.
[38] O.S. Alekseev, T. Beutel, E.A. Paukshtis, Y.A. Ryndin, V.A. Likholobov, H. Knözinger, FTIR studies of CO chemisorption and reactivity on Rh/SiO2 catalysts promoted by niobium oxide, J. Mol. Catal., 92 (1994) 217-233.
[39] J. Szanyi, J.H. Kwak, Dissecting the steps of CO2 reduction: 1. The interaction of CO and CO2 with [gamma]-Al2O3: an in situ FTIR study, PCCP, 16 (2014) 15117-15125.
[40] M. Dimitrakopoulou, X. Huang, J. Kröhnert, D. Teschner, S. Praetz, C. Schlesiger, W. Malzer, C. Janke, E. Schwab, F. Rosowski, H. Kaiser, S. Schunk, R. Schlögl, A. Trunschke, Insights into structure and dynamics of (Mn,Fe)Ox-promoted Rh nanoparticles, Faraday Discuss., 208 (2018) 207-225.
[41] K. Ding, D.A. Cullen, L. Zhang, Z. Cao, A.D. Roy, I.N. Ivanov, D. Cao, A general synthesis approach for supported bimetallic nanoparticles via surface inorganometallic chemistry, Science, 362 (2018) 560-564.
[42] A.B. Kroner, M.A. Newton, M. Tromp, A.E. Russell, A.J. Dent, J. Evans, Structural characterization of alumina-supported Rh catalysts: effects of ceriation and zirconiation by using metal-organic precursors, ChemPhysChem, 14 (2013) 3606-3617.
[43] N.M. Martin, F. Hemmingsson, X. Wang, L.R. Merte, U. Hejral, J. Gustafson, M. Skoglundh, D.M. Meira, A.-C. Dippel, O. Gutowski, M. Bauer, P.-A. Carlsson, Structure–function relationship during CO2 methanation over Rh/Al2O3 and Rh/SiO2 catalysts under atmospheric pressure conditions, Catal. Sci. Technol., 8 (2018) 2686-2696.
[44] J. Coey, The crystal structure of Rh2O3, Acta Crystallogr. B, 26 (1970) 1876-1877.
[45] S.L. Scott, A Matter of Life(time) and Death, ACS Catal., 8 (2018) 8597-8599.
[46] S. Eckle, Y. Denkwitz, R.J. Behm, Activity, selectivity, and adsorbed reaction intermediates/reaction side products in the selective methanation of CO in reformate gases on supported Ru catalysts, J. Catal., 269 (2010) 255-268.

[47] M. Calatayud, S.E. Collins, M.A. Baltanas, A.L. Bonivardi, Stability of formate species on [small beta]-Ga2O3, PCCP, 11 (2009) 1397-1405.
[48] L. Liu, C. Zhao, Y. Li, Spontaneous Dissociation of CO2 to CO on Defective Surface of Cu(I)/TiO2–x Nanoparticles at Room Temperature, J. Phys. Chem. C, 116 (2012) 7904-7912.
[49] Y. Lei, A. Uhl, C. Becker, K. Wandelt, B.C. Gates, R. Meyer, M. Trenary, Adsorption and reaction of Rh(CO)2(acac) on Al2O3/Ni3Al(111), PCCP, 12 (2010) 1264-1270.
[50] S. Ma, W. Song, B. Liu, H. Zheng, J. Deng, W. Zhong, J. Liu, X.-Q. Gong, Z. Zhao, Elucidation of the high CO2 reduction selectivity of isolated Rh supported on TiO2: a DFT study, Catal. Sci. Technol., 6 (2016) 6128-6136.

Graphical Abstract

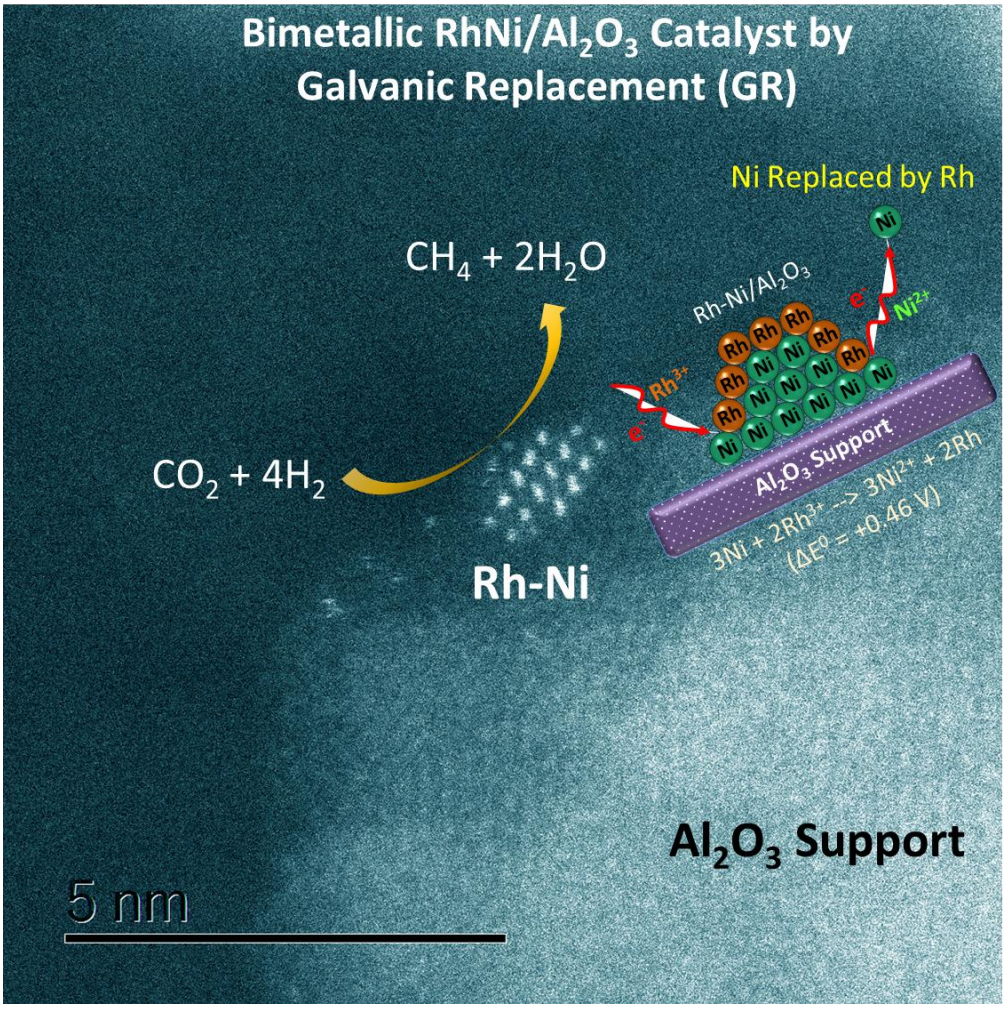

A bimetallic $RhNi/Al_2O_3$ catalyst prepared by galvanic replacement (GR) offers enhanced catalytic CO_2 hydrogenation to selectively produce methane.